Variation of convective heat flux imbalance with Prandtl number

By **M. Pathak, L. Sharma, H. Tiwari,** AND **M. K. Verma**†

We perform numerical simulations of compressible turbulent convection for Prandtl numbers (Pr) in the range (0.01, 100) and Rayleigh numbers (Ra) in the range ($10^7, 10^9$). We compute positive and negative heat fluxes and show them to be nearly equal. The difference between these fluxes scales as $Ra^{-0.20}$, leading to the classical Nu scaling, $Nu \sim Ra^{0.30}$, for all Pr. An exception to the above scaling is $Pr \leq 0.1$ in two dimensions, where Nu increases with Ra slower than the classical scaling.

1. Introduction

Turbulent thermal convection is a ubiquitous phenomenon that governs heat transport in a wide range of astrophysical and industrial systems, ranging from stellar and planetary interiors to devices such as boilers and heat exchangers (Siggia 1994; Ahlers *et al.* 2009; Chillà & Schumacher 2012; Verma 2018; Schumacher & Sreenivasan 2020). Understanding the mechanisms of turbulent convection is therefore essential for accurate modeling of these complex systems. A central quantity of interest in turbulent convection is the Nusselt number (Nu), which quantifies the convective heat transport relative to conduction. Despite extensive research, scaling the Nusselt number in turbulent thermal convection remains a significant challenge.

Extensive studies in recent years have used the canonical framework of Rayleigh–Bénard convection (RBC) to investigate turbulent heat transport, where a fluid layer is confined between two horizontal plates with the lower plate heated and the upper plate cooled (Siggia 1994; Ahlers *et al.* 2009; Verma 2018). RBC assumes the Boussinesq approximation, in which the fluid density is nearly constant, except for small variations in the buoyancy term, while other fluid parameters remain constant in space and time. However, the Boussinesq approximation is inapplicable to many geophysical and astrophysical applications because their density variations are of the order of their mean density (Spiegel & Veronis 1960; Cattaneo *et al.* 1991; Schumacher & Sreenivasan 2020; Ricard *et al.* 2022). The important nondimensional parameters of thermal convection are the Rayleigh number (Ra), which measures the relative strength of buoyancy to dissipative terms, and the Prandtl number (Pr), which is the ratio of viscous to thermal diffusivity. However, the scaling of Nu with Ra remains highly debated, with various theoretical and experimental studies reporting different results depending on Pr (Malkus 1954; Kraichnan 1962; Grossmann & Lohse 2000; Niemela *et al.* 2000; Chavanne *et al.* 2001; Zhu *et al.* 2018; Iyer *et al.* 2020; Lohse & Shishkina 2024).

There are two competing theories of Nu scaling in turbulent RBC. Based on the assumption of a marginally stable boundary layer and heat flux independence with box height, Malkus (1954), Spiegel (1962), and Priestley (1954) proposed the classical scaling $Nu \sim Ra^{1/3}$. In contrast, by using mixing-length and boundary layer theories, Kraichnan

---

† Indian Institute of Technology, Kanpur

(1962) predicted an ultimate regime in which both the bulk and boundary layers are turbulent, yielding a steeper scaling, $Nu \sim Ra^{1/2}$, for sufficiently high Ra. Grossmann & Lohse (2000) developed a phenomenological approach to predict Nu scaling based on the contributions from bulk and boundary layer dissipation. Numerical simulations and experiments have been performed to test the above scaling. Some researchers support the classical 1/3 scaling (Niemela *et al.* 2000; Urban *et al.* 2011; Iyer *et al.* 2020), whereas others report evidence for the ultimate 1/2 scaling (Chavanne *et al.* 2001; He *et al.* 2012; Zhu *et al.* 2018; Lohse & Shishkina 2024). The scaling behavior of Nu in compressible convection is relatively less well explored. John & Schumacher (2023a,b) and Tiwari *et al.* (2025a,b) simulated compressible convection for Ra up to 10^{16} in two dimensions (2D) and up to 10^{13} in three dimensions (3D) for $Pr \sim O(1)$, and reported that $Nu \sim Ra^{1/3}$.

A burning question in turbulent convection is which of the two phenomenologies applies to the system. Recent work by Tiwari *et al.* (2025b) offers valuable insight into this topic. These authors computed positive heat flux ($u_z T > 0$) and negative heat flux ($u_z T < 0$) in RBC and compressible convection up to $Ra = 10^{16}$ in 2D and 10^{13} in 3D for $Pr = 0.7$. Interestingly, for high Ra values, both positive and negative fluxes exhibit power-law variations with Ra, with the difference scaling as $Ra^{-0.20}$, which leads to the robust Nu scaling of $\sim Ra^{0.30}$. The emergence of near-equal positive and negative heat fluxes suggests isotropization of the turbulent convection. In this paper, we extend this analysis to Pr ranging from 0.01 to 100 in compressible convection.

Pr is an important parameter for Nu scaling in both RBC and compressible convection. In RBC, studies have reported that, for low-Pr convection ($Pr \ll 1$), Nu scales with Ra with an exponent typically in the range 0.20 to 0.25 (Cioni *et al.* 1997; Grossmann & Lohse 2000; Ahlers *et al.* 2009). For moderate- to high-Pr convection ($Pr \gtrsim 1$), the scaling exponent lies between 0.28 and 0.33 (Verzicco & Camussi 1999; Grossmann & Lohse 2000; Silano *et al.* 2010; Bhattacharya *et al.* 2021). Similar works for Pr dependence are relatively rare for compressible convection. Toomre *et al.* (1990), Singh & Chan (1993), Manga & Weeraratne (1999), and Käpylä (2021) have studied compressible convection with low Pr and high Pr, but a systematic analysis of Nu scaling for different Pr is still lacking. In this paper, we investigate the Pr dependence of Nu in compressible convection for Ra ranging from 10^7 to 10^9 and Pr ranging from 0.01 to 100.

This brief is organized as follows. In Section 2, we present the governing equations and discuss the heat flux. Section 3 describes the numerical simulation details. In Section 4, we investigate the imbalance between positive and negative heat fluxes for a range of Ra and Pr. We summarize our findings in Section 5.

2. Equations for compressible convection and and heat flux

The dynamics of a compressible fluid confined in a rectangular box subjected to an unstable vertical temperature gradient are governed by the conservation of mass, momentum, and energy. We denote the temperatures of the bottom and top plates using T_b and T_t, respectively, with $T_b > T_t$. In vector notation, these equations can be expressed in nondimensional conservative form as (Spiegel 1965; Graham 1975)

$$\frac{\partial \rho}{\partial t} + \nabla \cdot (\rho \mathbf{u}) = 0, \tag{2.1}$$

$$\frac{\partial (\rho \mathbf{u})}{\partial t} + \nabla \cdot \big(\rho \mathbf{u} \otimes \mathbf{u} + p\mathbf{I} - \boldsymbol{\tau}\big) = -\frac{1}{\epsilon}\rho \hat{\mathbf{z}}, \tag{2.2}$$

$$\frac{\partial E}{\partial t} + \nabla \cdot \Big[\mathbf{u}(E+p) - \frac{1}{\epsilon D\sqrt{RaPr}}\nabla T - \boldsymbol{\tau}\cdot \mathbf{u}\Big] = 0, \tag{2.3}$$

where ρ is the fluid density, $\mathbf{u} = (u, v, w)^T$ is the velocity vector, p is the pressure, $\mathbf{I}$ is the identity tensor, $\boldsymbol{\tau}$ is the viscous stress tensor, E is the total energy density, T is the temperature, and $\hat{\mathbf{z}}$ denotes the unit vector along the positive vertical direction. Note that all the fields are expressed in nondimensional form using the characteristic scales: fluid height d for length, $\sqrt{\epsilon g d}$ for velocity, ρ_b for density, and T_b for temperature. Here, g is the gravitational acceleration along the $-\hat{\mathbf{z}}$ direction and ρ_b is the density at the bottom plate. The fluid is assumed to follow the ideal gas equation of state.

The nondimensional parameters characterizing the system are the Rayleigh number (Ra), Prandtl number (Pr), dissipation number (D), and superadiabaticity (ϵ), which are defined as (Verhoeven *et al.* 2015; John & Schumacher 2023b)

$$Ra = \frac{\epsilon g d^3}{\nu \kappa}, \qquad Pr = \frac{\nu}{\kappa}, \qquad D = \frac{gd}{T_b C_p}, \qquad \epsilon = \frac{d}{T_b}\left(\frac{\Delta}{d} - \frac{g}{C_p}\right). \tag{2.4}$$

Here, μ is the constant dynamic viscosity, K is the thermal conductivity, C_p is the specific heat capacity at constant pressure, $\nu = \mu/\rho$ is the kinematic viscosity, and $\kappa = K/C_p\rho$ is the thermal diffusivity of the fluid. The imposed vertical temperature gradient is $\Delta = (T_b - T_t)/d$. The aspect ratio $\Gamma = L/d$ (where L is the length of the rectangular box) and the specific heat capacity ratio $\gamma = C_p/C_v$ (where C_v is the specific heat capacity at constant volume) are also important parameters of the system.

The background adiabatic profile is $T_A(z) = 1 - Dz$. The superadiabatic temperature, defined as the deviation of the actual temperature field from this adiabatic profile, $T_{\rm sa}(\mathbf{r}, t) = T(\mathbf{r}, t) - T_A(z)$, quantifies the excess thermal driving beyond the adiabatic stratification. All field variables are taken to be periodic in the horizontal direction. Along the vertical direction, the temperatures are fixed, while velocity satisfies the no-slip boundary conditions

$$\mathbf{u}(z = 0, 1) = 0, \qquad T(z = 0) = 1, \qquad T(z = 1) = 1 - D - \epsilon. \tag{2.5}$$

Nondimensional convective heat transport is the Nusselt number (Nu), which is (Graham 1975; Tiwari *et al.* 2025a)

$$Nu = 1 + \frac{\sqrt{RaPr}}{\epsilon}\langle \rho u_z T_{\rm sa}\rangle + \frac{D\sqrt{RaPr}}{2}\langle \rho u_z u^2\rangle = 1 + Nu_{\rm conv} + Nu_K. \tag{2.6}$$

Here, $Nu_{\rm conv}$ and Nu_K represent the convective and kinetic contributions, respectively, and $\langle\cdot\rangle$ is the combined volume–time average. Note that, as reported by Tiwari *et al.* (2025a), $Nu_K \ll Nu_{\rm conv}$. Thus, we can safely ignore the kinetic contributions to Nu, so Eq. (2.6) becomes

$$Nu = 1 + \frac{\sqrt{RaPr}}{\epsilon}\langle \rho u_z T_{\rm sa}\rangle = 1 + \frac{\sqrt{RaPr}}{\epsilon}\langle F_z\rangle, \tag{2.7}$$

where $\langle F_z\rangle$ denotes the net vertical heat flux. As discussed by Tiwari *et al.* (2025b), for $Pr = 0.7$, turbulent convection exhibits positive and negative fluxes, F_{z+} and F_{z-}, respectively. They are defined as (Graham 1975; Tiwari *et al.* 2025a)

$$Nu = 1 + \frac{\sqrt{RaPr}}{\epsilon}[\langle F_{z+}\rangle + \langle F_{z-}\rangle] = 1 + \frac{\sqrt{RaPr}}{\epsilon}\Big[\langle(\rho u_z T_{\rm sa})_+\rangle + \langle(\rho u_z T_{\rm sa})_-\rangle\Big]. \tag{2.8}$$

The total heat flux, $\langle F_z\rangle$, which is related to Nu, thus receives contributions from both positive and negative heat fluxes $\langle F_{z\pm}\rangle$. Tiwari *et al.* (2025b) showed that $\langle F_{z+}\rangle$ dominates $\langle F_{z-}\rangle$, resulting in a net positive heat flux. In this paper, we extend the analysis presented by Tiwari *et al.* (2025b) to a range of Pr.

The volume or bulk Nu shows significant fluctuations (Pandey & Sreenivasan 2025). Therefore, we also use another definition of Nu, called boundary Nu, which shows less fluctuation and is computed using the heat flux at the top and bottom boundaries

$$Nu = -\frac{1}{2}\left[\left.\frac{d\langle T_{\rm sa}\rangle_{A,t}}{dz}\right|_{z=0} + \left.\frac{d\langle T_{\rm sa}\rangle_{A,t}}{dz}\right|_{z=1}\right], \tag{2.9}$$

where $\langle\cdot\rangle_{A,t}$ represents the combined planar and temporal average. Both definitions result in nearly identical values if averaged sufficiently. Note, however, that bulk-averaged Nu in 2D exhibits strong fluctuations, which poses a significant computational challenge (Pandey & Sreenivasan 2025). In the next section, we describe the numerical method and the simulation parameters.

3. Numerical simulation details

The governing equations (Eqs. (2.1)-(2.3)) are solved numerically using the finite-difference solver Dhara (Tiwari *et al.* 2025a). The code employs a collocated grid and advances the solution using the MacCormack predictor–corrector method supplemented with a total variation diminishing (TVD) scheme (Yee 1987; Wesseling 2000; Liang *et al.* 2007; Ouyang *et al.* 2013). The MacCormack scheme ensures second-order accuracy in both space and time, while the TVD flux limiter suppresses spurious oscillations and maintains monotonicity in regions with sharp gradients. Our scheme is less accurate compared with the sixth-order compact scheme (Lele 1992). However, the large-scale quantities like Nu and Re show good agreement with the benchmark data. With sufficient grid resolution, our second-order scheme accurately captures the large-scale structures, thereby ensuring the fidelity of the reported Nu values. For computing the fields near the boundaries, we employ second-order forward and backward finite-difference schemes at the bottom and top plates, respectively. To achieve adequate resolution near the boundary layers, we use either a uniform or a tangent–hyperbolic stretched nonuniform grid in the vertical (z) direction, depending on the control parameters. We employ uniform spacing in the horizontal directions. Refer to Tiwari *et al.* (2025a) for more details.

We perform direct numerical simulations in 2D and 3D at $Ra = 10^7$, 10^8, and 10^9. We consider no-slip boundary conditions for the velocity field and perfectly conducting boundaries for the temperature field on both the top and bottom plates. Periodic boundary conditions are applied along the sidewalls. We use some of the datasets from Sharma *et al.* (2025) for $Pr = 0.01$, 0.1, and 100 and carry out new numerical simulations for $Pr = 1$ and 10. To reduce statistical errors at high Pr, we perform two additional runs at $Ra = 5 \times 10^7$ and 5×10^8 for $Pr = 100$. For all our simulations, we fix the other parameters to $\epsilon = 0.1$, $D = 0.5$, $\gamma = 1.3$, and $\Gamma = 1$. Table 1 lists the values of Ra and Pr, grid sizes, values of the boundary Nu, and magnitudes of the mean positive and

Run	Ra	Pr	Grid size	Nu	$\lvert\langle F_{z+}\rangle\rvert$	$\lvert\langle F_{z-}\rangle\rvert$
3D						
1	10^7	0.01	401^3	3.92 ± 0.23	1.6×10^{-3}	5.3×10^{-4}
2	10^7	0.1	257^3	6.32 ± 0.29	1.1×10^{-3}	4.7×10^{-4}
3	10^7	1	257^3	8.38 ± 0.38	6.6×10^{-4}	3.9×10^{-4}
4	10^7	10	257^3	9.35 ± 0.32	3.1×10^{-4}	2.3×10^{-4}
5	10^7	100	257^3	9.22 ± 0.17	9.5×10^{-5}	6.9×10^{-5}
6	10^8	0.01	401^3	7.26 ± 0.14	1.3×10^{-3}	4.7×10^{-4}
7	10^8	0.1	257^3	11.30 ± 0.43	8.9×10^{-4}	4.8×10^{-4}
8	10^8	1	257^3	14.97 ± 0.51	5.5×10^{-4}	3.9×10^{-4}
9	10^8	10	257^3	16.56 ± 0.52	2.7×10^{-4}	2.2×10^{-4}
10	10^8	100	257^3	17.47 ± 0.23	1.0×10^{-4}	8.6×10^{-5}
11	10^9	0.01	701^3	13.97 ± 0.52	1.0×10^{-3}	5.0×10^{-4}
12	10^9	0.1	701^3	21.83 ± 0.79	7.4×10^{-4}	4.7×10^{-4}
13	10^9	1	513^3	28.47 ± 0.69	4.6×10^{-4}	3.6×10^{-4}
14	10^9	10	513^3	30.88 ± 0.61	2.8×10^{-4}	2.5×10^{-4}
15	10^9	100	513^3	32.76 ± 0.87	9.1×10^{-5}	8.1×10^{-5}
16	5×10^7	100	257^3	13.99 ± 0.23	9.6×10^{-5}	7.8×10^{-5}
17	5×10^8	100	257^3	27.83 ± 0.66	9.3×10^{-5}	8.0×10^{-5}
2D						
18	10^7	0.01	1501^2	8.89 ± 0.29	5.5×10^{-3}	2.7×10^{-3}
19	10^7	0.1	513^2	7.74 ± 0.40	2.1×10^{-3}	1.3×10^{-3}
20	10^7	1	257^2	6.72 ± 0.77	9.4×10^{-4}	7.0×10^{-4}
21	10^7	10	257^2	7.56 ± 0.60	3.1×10^{-4}	2.4×10^{-4}
22	10^7	100	257^2	8.04 ± 0.10	1.1×10^{-4}	8.7×10^{-5}
23	10^8	0.01	2049^2	11.33 ± 2.07	3.5×10^{-3}	2.7×10^{-3}
24	10^8	0.1	513^2	11.83 ± 1.24	1.9×10^{-3}	1.6×10^{-3}
25	10^8	1	257^2	12.31 ± 0.50	9.0×10^{-4}	7.5×10^{-4}
26	10^8	10	257^2	14.07 ± 0.81	3.7×10^{-4}	3.2×10^{-4}
27	10^8	100	257^2	14.82 ± 0.86	1.0×10^{-4}	8.7×10^{-5}
28	10^9	0.01	3001^2	16.58 ± 1.36	2.4×10^{-3}	1.8×10^{-3}
29	10^9	0.1	1001^2	19.69 ± 0.75	1.8×10^{-3}	1.6×10^{-3}
30	10^9	1	513^2	22.78 ± 1.43	9.3×10^{-4}	8.5×10^{-4}
31	10^9	10	513^2	27.53 ± 1.99	4.8×10^{-4}	4.5×10^{-4}
32	10^9	100	513^2	28.69 ± 0.69	1.5×10^{-4}	1.4×10^{-4}
33	5×10^7	100	257^2	12.15 ± 0.64	1.1×10^{-4}	9.0×10^{-5}
34	5×10^8	100	257^2	23.29 ± 1.17	1.3×10^{-4}	1.2×10^{-4}

TABLE 1. Simulation parameters: Rayleigh number Ra, Prandtl number Pr, grid size, Nusselt number Nu, and absolute values of mean positive and negative vertical heat fluxes ($|\langle F_{z+}\rangle|$, $|\langle F_{z-}\rangle|$). Also, superadiabaticity $\epsilon = 0.1$, dissipation number $D = 0.5$, aspect ratio $\Gamma = 1$, and ratio of specific heats $\gamma = 1.3$.

negative fluxes ($|\langle F_{z+}\rangle|$, $|\langle F_{z-}\rangle|$). We compute Nu using Eq. (2.9) and average it over 2000 to 10,000 data frames in the steady state. We compute $|\langle F_{z+}\rangle|$ and $|\langle F_{z-}\rangle|$ by time averaging over 20 to 30 snapshots. Our simulations are well resolved in both the bulk

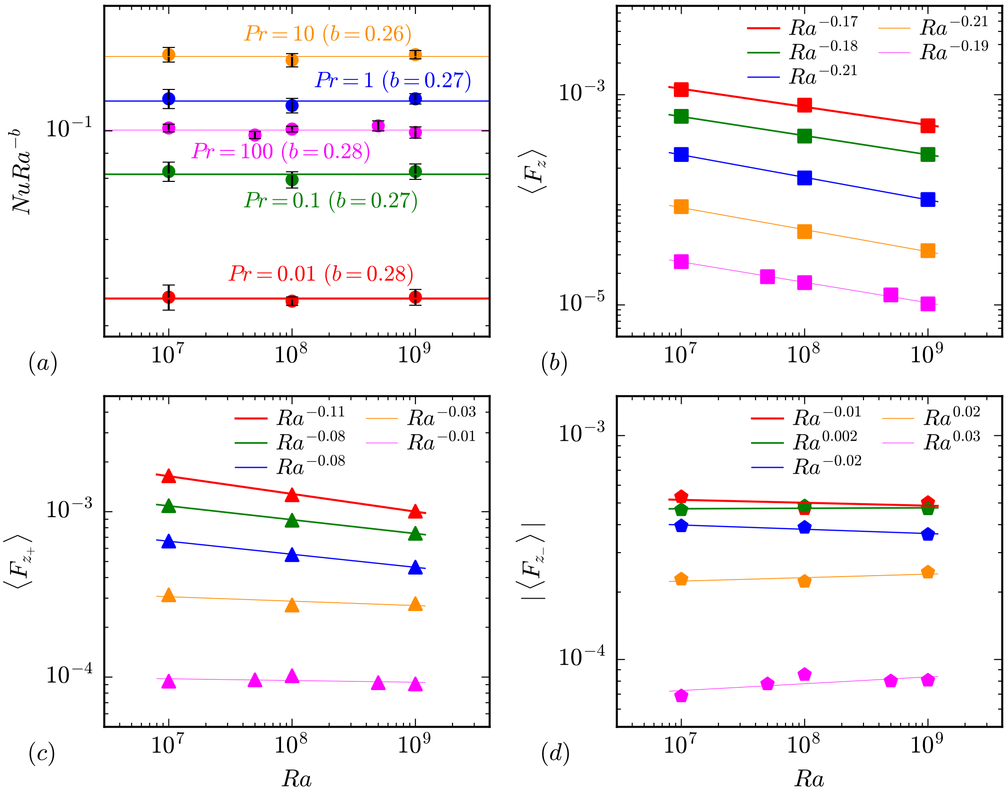

FIGURE 1. For 3D convection, plots of (a) normalized Nusselt number $NuRa^{-b}$, (b) total heat flux $\langle F_z \rangle$, (c) positive heat flux $\langle F_{z+} \rangle$, and (d) absolute negative heat flux $|\langle F_{z-} \rangle|$ as a function of Ra, with $Pr = 0.01$ (red), 0.1 (green), 1 (blue), 10 (orange), and 100 (magenta). Panel a models $Nu = aRa^b$.

and the boundary layer, with at least five grid points in the boundary, thereby satisfying the Grötzbach resolution criterion (Grötzbach 1983; Tiwari *et al.* 2025a). The following section discusses the imbalance of positive and negative heat fluxes for a range of Ra and Pr.

4. Positive and negative heat fluxes

In this section, we investigate Nu–Ra scaling for various Pr. As in earlier literature, we model $Nu = a(Ra)^b$, where a and b are the prefactor and the scaling exponent, respectively. The parameters a and b were computed using the polyfit function of Python. Figures 1(a) and 2(a) exhibit the normalized function $NuRa^{-b}$ for $Pr = 0.01, 0.1, 1, 10,$ and 100 in 3D and 2D, respectively. Figures 1(b) and 2(b) show the scaling of the total (normalized) heat flux, $\langle F_z \rangle$, for 3D and 2D, respectively. Note that the total flux is averaged over 20 to 30 snapshots. Table 2 summarizes the scaling of Nu and $\langle F_z \rangle$ for different Pr.

First, we discuss the Nu scaling for 3D convection. Here, for all Pr, Figure 1(a) illustrates that $Nu \sim Ra^{0.27}$, which is close to the classical scaling $Nu \sim Ra^{1/3}$. The prefactor a increases from 0.045 to 0.082 for $Pr < 1$, while a is close to $\sim$0.1 for $Pr \geq 1$. See Ta-

Pr	Nu	$\langle F_z \rangle$
	3D	
0.01	$(4.54 \pm 0.39) \times 10^{-2}\, Ra^{(0.28 \pm 0.005)}$	$(1.82 \pm 0.47) \times 10^{-2}\, Ra^{(-0.17 \pm 0.01)}$
0.1	$(8.15 \pm 1.46) \times 10^{-2}\, Ra^{(0.27 \pm 0.01)}$	$(1.15 \pm 0.08) \times 10^{-2}\, Ra^{(-0.18 \pm 0.004)}$
1	$(1.15 \pm 0.17) \times 10^{-1}\, Ra^{(0.27 \pm 0.01)}$	$(8.45 \pm 0.89) \times 10^{-3}\, Ra^{(-0.21 \pm 0.01)}$
10	$(1.42 \pm 0.17) \times 10^{-1}\, Ra^{(0.26 \pm 0.01)}$	$(2.46 \pm 0.74) \times 10^{-3}\, Ra^{(-0.21 \pm 0.02)}$
100	$(1.00 \pm 0.10) \times 10^{-1}\, Ra^{(0.28 \pm 0.01)}$	$(5.90 \pm 0.81) \times 10^{-4}\, Ra^{(-0.19 \pm 0.01)}$
	2D	
0.01	$(9.82 \pm 3.16) \times 10^{-1}\, Ra^{(0.14 \pm 0.02)}$	$(6.36 \pm 12.38) \times 10^{-1}\, Ra^{(-0.34 \pm 0.11)}$
0.1	$(2.91 \pm 0.58) \times 10^{-1}\, Ra^{(0.20 \pm 0.01)}$	$(1.22 \pm 0.51) \times 10^{-1}\, Ra^{(-0.31 \pm 0.02)}$
1	$(9.35 \pm 0.22) \times 10^{-2}\, Ra^{(0.27 \pm 0.001)}$	$(8.98 \pm 2.56) \times 10^{-3}\, Ra^{(-0.23 \pm 0.02)}$
10	$(8.12 \pm 0.95) \times 10^{-2}\, Ra^{(0.28 \pm 0.01)}$	$(1.20 \pm 0.48) \times 10^{-3}\, Ra^{(-0.18 \pm 0.02)}$
100	$(9.13 \pm 0.77) \times 10^{-2}\, Ra^{(0.28 \pm 0.005)}$	$(5.49 \pm 1.46) \times 10^{-4}\, Ra^{(-0.20 \pm 0.01)}$

TABLE 2. For 3D and 2D turbulent convection, scaling of Nu and total vertical heat flux $\langle F_z \rangle$ with Ra for different Pr.

ble 4 for the trends of the prefactor and the scaling exponents. We compute the total normalized vertical heat flux using Eq. (2.7) and observe $\langle F_z \rangle \sim NuRa^{-1/2} \sim Ra^{b-1/2}$. Since $b \approx 0.27$ for all Pr, $\langle F_z \rangle \approx Ra^{-0.23}$, which is nearly borne out in our simulations, as illustrated in Figure 1(b). Verma *et al.* (2012) and Pandey & Verma (2016) have shown that $\langle F_z \rangle \approx Ra^{-0.20}$, which is similar to the scaling presented in this paper.

To further understand the dynamics of heat transport and isotropization, we compute the positive and negative vertical heat fluxes, $\langle F_{z\pm} \rangle$, using numerical data. The heat fluxes follow $\langle F_{z\pm} \rangle = a_\pm Ra^{b_\pm}$, as illustrated in Figure 1(c,d). The corresponding scaling is also listed in Table 3, and the trends are shown in Table 4. We observe that the exponent b_+ increases from -0.11 to -0.01 with the increase of Pr from 0.01 to 100, whereas b_- is nearly zero for all Pr. However, the difference between the two fluxes, $\langle F_z \rangle$, scales nearly as $Ra^{-0.20}$, which yields approximate classical scaling for Nu ($Nu \sim Ra^{0.28}$).

We now discuss the positive and negative heat fluxes in 2D convection. Figure 2(a, b) illustrates $NuRa^{-b}$ and $\langle F_z \rangle$ as a function of Ra for various Pr. Also see Table 2 for the corresponding scaling. For moderate to high Pr ($Pr \geq 1$), $Nu \sim Ra^{0.28}$ and $\langle F_z \rangle \sim Ra^{-0.20}$. However, for low Pr ($Pr < 1$), the Nu scaling exponent, b, increases from 0.14 to 0.20, consistent with earlier results (Cioni *et al.* 1997; Grossmann & Lohse 2000; Ahlers *et al.* 2009). Thus, for low Pr, $\langle F_z \rangle$ scales faster than $Ra^{-0.20}$. The prefactor $a \approx 0.1$ for $Pr \geq 1$, but it varies from 0.29 to 0.98 for $Pr \leq 0.1$.

For 2D, Figure 2(c,d) exhibits the scaling of the positive and negative fluxes, $\langle F_{z\pm} \rangle$, with Ra at different Pr. The corresponding scaling and its trends are summarized in Tables 3 and 4, respectively. Note that b_+ increases from -0.19 to 0.10, whereas b_- increases from -0.09 to 0.14. However, the positive heat flux wins over the negative flux for all Pr. For $Pr \geq 1$, the small difference in the heat flux scales nearly as $Ra^{-0.20}$, resulting in $Nu \sim Ra^{0.30}$. However, for $Pr \leq 0.1$, Nu increases more slowly than classical scaling.

Pr	$\|\langle F_{z+}\rangle\|$	$\|\langle F_{z-}\rangle\|$
	3D	
0.01	$(9.21 \pm 0.78) \times 10^{-3}\, Ra^{(-0.11\pm0.005)}$	$(6.37 \pm 2.77) \times 10^{-4}\, Ra^{(-0.01\pm0.02)}$
0.1	$(4.18 \pm 0.20) \times 10^{-3}\, Ra^{(-0.08\pm0.003)}$	$(4.55 \pm 0.73) \times 10^{-4}\, Ra^{(0.002\pm0.009)}$
1	$(2.36 \pm 0.08) \times 10^{-3}\, Ra^{(-0.08\pm0.002)}$	$(5.42 \pm 0.72) \times 10^{-4}\, Ra^{(-0.02\pm0.01)}$
10	$(4.70 \pm 1.76) \times 10^{-4}\, Ra^{(-0.03\pm0.02)}$	$(1.74 \pm 0.48) \times 10^{-4}\, Ra^{(0.02\pm0.01)}$
100	$(1.16 \pm 0.27) \times 10^{-4}\, Ra^{(-0.01\pm0.01)}$	$(4.44 \pm 1.54) \times 10^{-5}\, Ra^{(0.03\pm0.02)}$
	2D	
0.01	$(1.08 \pm 0.12) \times 10^{-1}\, Ra^{(-0.19\pm0.01)}$	$(1.23 \pm 1.16) \times 10^{-2}\, Ra^{(-0.09\pm0.05)}$
0.1	$(3.39 \pm 0.30) \times 10^{-3}\, Ra^{(-0.03\pm0.005)}$	$(5.98 \pm 1.96) \times 10^{-4}\, Ra^{(0.05\pm0.02)}$
1	$(9.50 \pm 1.51) \times 10^{-4}\, Ra^{(-0.002\pm0.009)}$	$(3.66 \pm 0.39) \times 10^{-4}\, Ra^{(0.04\pm0.01)}$
10	$(6.54 \pm 1.46) \times 10^{-5}\, Ra^{(0.10\pm0.01)}$	$(2.64 \pm 0.12) \times 10^{-5}\, Ra^{(0.14\pm0.003)}$
100	$(2.95 \pm 1.86) \times 10^{-5}\, Ra^{(0.07\pm0.03)}$	$(1.29 \pm 0.80) \times 10^{-5}\, Ra^{(0.11\pm0.03)}$

TABLE 3. For 3D and 2D turbulent convection, scaling of absolute values of the averaged positive and negative heat fluxes ($|\langle F_{z+}\rangle|$, $|\langle F_{z-}\rangle|$) with Ra for different Pr.

Quantities	$Pr < 1$	$Pr \geq 1$
	3D	
Nu	a increases from 0.045 to 0.082; $b \sim 0.27$	$a \approx 0.1$; $b \sim 0.27$
$\langle F_{z+}\rangle$	b_+ increases from -0.11 to -0.08	b_+ increases from -0.08 to -0.01
$\|\langle F_{z-}\rangle\|$	$b_- \sim -0.01$	b_- increases from -0.02 to 0.03
	2D	
Nu	a decreases from 0.98 to 0.29; b increases from 0.14 to 0.20	$a \approx 0.1$; $b \sim 0.28$
$\langle F_{z+}\rangle$	b_+ increases from -0.19 to -0.03	b_+ increases from -0.002 to 0.07
$\|\langle F_{z-}\rangle\|$	b_- increases from -0.09 to 0.05	b_- increases from 0.04 to 0.11

TABLE 4. For 3D and 2D turbulent convection, trend of Nu and ($|\langle F_{z+}\rangle|$, $|\langle F_{z-}\rangle|$) variations with Ra for $Pr < 1$ and $Pr \geq 1$. Here, $Nu = aRa^b$ and $\langle F_{z\pm}\rangle = a_\pm Ra^{b_\pm}$.

5. Conclusions

In this paper, we investigate the scaling of heat transport in 2D and 3D compressible turbulent convection. We vary Pr from 0.01 to 100 and Ra from 10^7 to 10^9, while other parameters are kept fixed. The net vertical heat flux takes both positive and negative values, but the positive flux ($\langle F_{z+}\rangle$) dominates the negative flux ($\langle F_{z-}\rangle$), leading to a net positive heat flux.

In 3D, Nu exhibits a nearly universal classical scaling, $Nu \sim Ra^{0.27}$, largely independent of Pr, while the net heat flux decreases approximately as $\langle F_z\rangle \sim Ra^{-0.20}$. The positive flux $\langle F_{z+}\rangle$ decreases faster than the negative flux $\langle F_{z-}\rangle$ for $Pr \leq 1$, whereas $\langle F_{z+}\rangle$ and $\langle F_{z-}\rangle$ are nearly independent for $Pr > 1$. In 2D, for moderate to high Pr, Nu scales as $Ra^{0.28}$ and the vertical flux $\langle F_z\rangle \sim Ra^{-0.20}$, similar to the 3D case. However, for low Pr, Nu is reduced in comparison to classical scaling ($Nu \sim Ra^{1/3}$), with the Nu

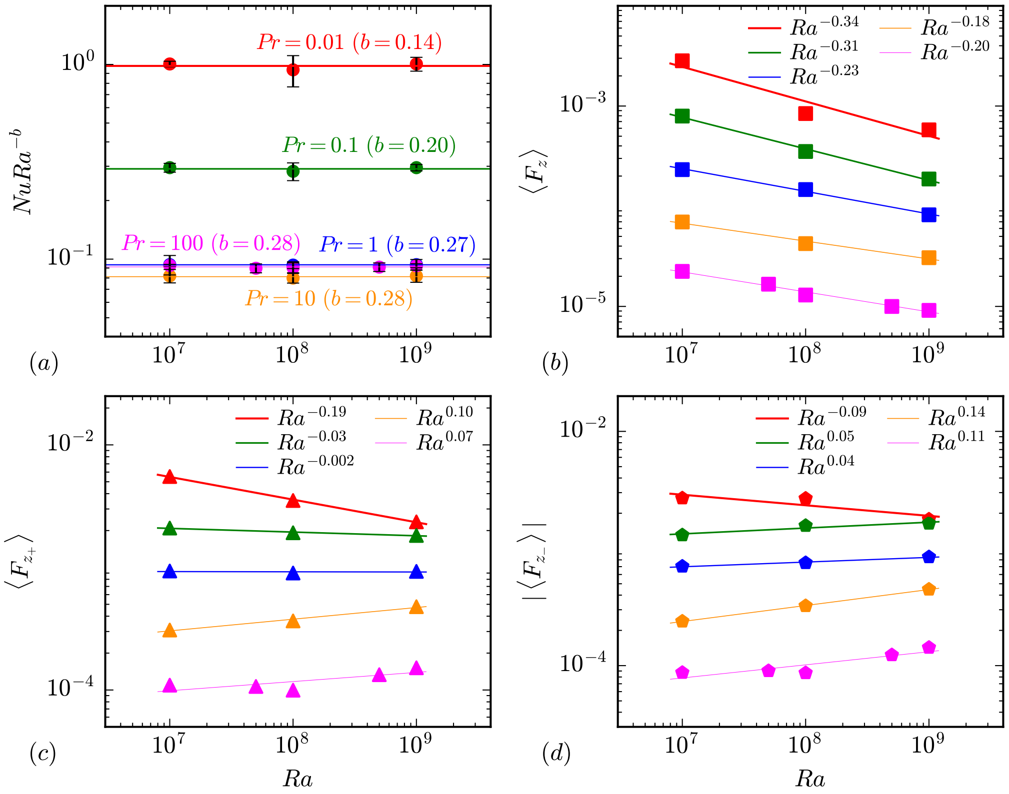

FIGURE 2. For 2D convection, scaling of (a) normalized Nusselt number $NuRa^{-b}$, (b) total heat flux $\langle F_z \rangle$, (c) positive heat flux $\langle F_{z+} \rangle$, and (d) absolute negative heat flux $|\langle F_{z-} \rangle|$ as a function of Ra. Color coding is the same as in Figure 1.

exponent ranging from 0.14 to 0.20. The positive and negative fluxes exhibit complex variation, as shown in Figure 2(c,d).

The ultimate regime ($Nu \sim Ra^{1/2}$) predicted by Kraichnan (1962) appears to indicate near-isotropic turbulent convection. Recently, Tiwari *et al.* (2025b) showed that for large Ra and $Pr = 0.7$, positive and negative heat fluxes attempt to cancel each other because of near isotropy. The difference between the positive flux and negative flux yields $Nu \sim Ra^{0.30}$, the classical scaling. In this paper, we extend the heat flux computations to $Pr = 0.01, 0.1, 1, 10$, and 100 and observe behavior similar to that reported earlier for $Pr = 0.7$ (Tiwari *et al.* 2025b). Earlier literature reported an increase in the Nu exponent for turbulent convection with rough walls (Roche *et al.* 2001) and horizontal shear (Pirozzoli *et al.* 2017). Therefore, we plan to compute the asymmetry in positive and negative heat fluxes in these systems. Such studies will provide valuable insights into heat transport in turbulent convection.

Acknowledgments

The authors thank Sanjiva Lele, Parviz Moin, Hang Song, Makrand Khanwale, Shashwat Bhattacharya, and Ambrish Pandey for useful discussions. The authors acknowledge computational resources from Argonne Leadership Computing Facility for the computer time through the Director's Discretionary Program. Simulations were performed on Polaris, Param Sanganak, and our laboratory GPUs. L.S. thanks the Indian Institute of Technology Kanpur for the Institute Postdoctoral Fellowship. Part of this work was done at the Center for Turbulence Research, Stanford University, where M.K.V. was a Visiting Senior Fellow, and was supported by the Anusandhan National Research Foundation, India (SERB/PHY/2021522), and a J. C. Bose Fellowship (SERB/PHY/2023488).

REFERENCES

Ahlers, G., Grossmann, S. & Lohse, D. 2009 Heat transfer and large scale dynamics in turbulent Rayleigh–Bénard convection. *Rev. Mod. Phys.* **81**, 503–537.

Bhattacharya, S., Verma, M. K. & Samtaney, R. 2021 Revisiting Reynolds and Nusselt numbers in turbulent thermal convection. *Phys. Fluids* **33**, 015113.

Cattaneo, F., Brummell, N. H., Toomre, J., Malagoli, A. & Hurlburt, N. E. 1991 Turbulent compressible convection. *Astrophys. J.* **370**, 282–294.

Chavanne, X., Chillà, F., Chabaud, B., Castaing, B. & Hebral, B. 2001 Turbulent Rayleigh–Bénard convection in gaseous and liquid He. *Phys. Fluids* **13**, 1300–1320.

Chillà, F. & Schumacher, J. 2012 New perspectives in turbulent Rayleigh–Bénard convection. *Eur. Phys. J. E* **35**, 58.

Cioni, S., Ciliberto, S. & Sommeria, J. 1997 Strongly turbulent Rayleigh–Bénard convection in mercury: comparison with results at moderate Prandtl number. *J. Fluid Mech.* **335**, 111–140.

Graham, E. 1975 Numerical simulation of two-dimensional compressible convection. *J. Fluid Mech.* **70**, 689–703.

Grossmann, S. & Lohse, D. 2000 Scaling in thermal convection: a unifying theory. *J. Fluid Mech.* **407**, 27–56.

Grötzbach, G. 1983 Spatial resolution requirements for direct numerical simulation of the Rayleigh–Bénard convection. *J. Comput. Phys.* **49**, 241–264.

He, X., Funfschilling, D., Nobach, H., Bodenschatz, E. & Ahlers, G. 2012 Transition to the ultimate state of turbulent Rayleigh–Bénard convection. *Phys. Rev. Lett.* **108**, 024502.

Iyer, K. P., Scheel, J. D., Schumacher, J. & Sreenivasan, K. R. 2020 Classical 1/3 scaling of convection holds up to $\mathrm{Ra} = 10^{15}$. *Proc. Natl. Acad. Sci. USA* **117**, 7594–7598.

John, J. P. & Schumacher, J. 2023a Compressible turbulent convection in highly stratified adiabatic background. *J. Fluid Mech.* **972**, R4.

John, J. P. & Schumacher, J. 2023b Strongly superadiabatic and stratified limits of compressible convection. *Phys. Rev. Fluids* **8**, 103505.

Käpylä, P. J. 2021 Prandtl number dependence of stellar convection: flow statistics and convective energy transport. *Astron. Astrophys.* **655**, A78.

Kraichnan, R. H. 1962 Turbulent thermal convection at arbitrary Prandtl number. *Phys. Fluids* **5**, 1374–1389.

Lele, S. K. 1992 Compact finite difference schemes with spectral-like resolution. *J. Comput. Phys.* **103**, 16–42.

Liang, D., Lin, B. & Falconer, R. A. 2007 Simulation of rapidly varying flow using an efficient TVD-MacCormack scheme. *Int. J. Numer. Methods Fluids* **53**, 811–826.

Lohse, D. & Shishkina, O. 2024 Ultimate Rayleigh–Bénard turbulence. *Rev. Mod. Phys.* **96**, 035001.

Malkus, W. V. R. 1954 The heat transport and spectrum of thermal turbulence. *Proc. R. Soc. Lond. A* **225**, 196–212.

Manga, M. & Weeraratne, D. 1999 Experimental study of non-Boussinesq Rayleigh–Bénard convection at high Rayleigh and Prandtl numbers. *Phys. Fluids* **11**, 2969–2976.

Niemela, J. J., Skrbek, L., Sreenivasan, K. R. & Donnelly, R. J. 2000 Turbulent convection at very high Rayleigh numbers. *Nature* **404**, 837–840.

Ouyang, C., He, S., Xu, Q., Luo, Y. & Zhang, W. 2013 A MacCormack-TVD finite difference method to simulate the mass flow in mountainous terrain with variable computational domain. *Comput. Geosci.* **52**, 1–10.

Pandey, A. & Sreenivasan, K. R. 2025 Transient and steady convection in two dimensions. *J. Fluid Mech.* **1015**, A42.

Pandey, A. & Verma, M. K. 2016 Scaling of large-scale quantities in Rayleigh–Bénard convection. *Phys. Fluids* **28**, 095105.

Pirozzoli, S., Bernardini, M., Verzicco, R. & Orlandi, P. 2017 Mixed convection in turbulent channels with unstable stratification. *J. Fluid Mech.* **821**, 482–516.

Priestley, C. 1954 Convection from a large horizontal surface. *Aust. J. Phys.* **7**, 176–201.

Ricard, Y., Alboussière, T., Labrosse, S., Curbelo, J. & Dubuffet, F. 2022 Fully compressible convection for planetary mantles. *Geophys. J. Int.* **230**, 932–956.

Roche, P.-E., Castaing, B., Chabaud, B. & Hebral, B. 2001 Observation of the 1/2 power law in Rayleigh–Bénard convection. *Phys. Rev. E* **63**, 045303(R).

Schumacher, J. & Sreenivasan, K. R. 2020 Colloquium: unusual dynamics of convection in the Sun. *Rev. Mod. Phys.* **92**, 041001.

Sharma, L., Pathak, M., Tiwari, H. & Verma, M. K. 2025 Prandtl number dependence in turbulent compressible convection. *Phys. Rev. Fluids* **10**, 114611.

Siggia, E. D. 1994 High Rayleigh number convection. *Annu. Rev. Fluid Mech.* **26**, 137–168.

Silano, G., Sreenivasan, K. R. & Verzicco, R. 2010 Numerical simulations of Rayleigh–Bénard convection for Prandtl numbers between 10^{-1} and 10^4 and Rayleigh numbers between 10^5 and 10^9. *J. Fluid Mech.* **662**, 409–446.

Singh, H. P. & Chan, K. L. 1993 A study of the three-dimensional turbulent compressible convection in a deep atmosphere at various Prandtl numbers. *Astron. Astrophys.* **279**, 107–118.

Spiegel, E. A. 1962 On the Malkus theory of turbulence. In *Mécanique de la Turbulence*, pp. 181–201. Gordon & Breach

Spiegel, E. A. 1965 Convective instability in a compressible atmosphere. I. *Astrophys. J.* **141**, 1068–1090.

Spiegel, E. A. & Veronis, G. 1960 On the Boussinesq approximation for a compressible fluid. *Astrophys. J.* **131**, 442–447.

Tiwari, H., Sharma, L. & Verma, M. K. 2025a Compressible turbulent convection at very high Rayleigh numbers. *Int. J. Heat Mass Transf.* **242**, 126821.

Tiwari, H., Sharma, L. & Verma, M. K. 2025b On the absence of the ultimate regime in turbulent thermal convection. *Proc. Natl. Acad. Sci. USA* **122**, e2513474122.

Toomre, J., Brummell, N., Cattaneo, F. & Hurlburt, N. E. 1990 Three-dimensional compressible convection at low Prandtl numbers. *Comput. Phys. Commun.* **59**, 105–117.

Urban, P., Musilová, V. & Skrbek, L. 2011 Efficiency of heat transfer in turbulent Rayleigh–Bénard convection. *Phys. Rev. Lett.* **107**, 014302.

Verhoeven, J., Wiesehöfer, T. & Stellmach, S. 2015 Anelastic versus fully compressible turbulent Rayleigh–Bénard convection. *Astrophys. J.* **805**, 62.

Verma, M. K. 2018 *Physics of Buoyant Flows: From Instabilities to Turbulence*. World Scientific.

Verma, M. K., Mishra, P. K., Pandey, A. & Paul, S. 2012 Scalings of field correlations and heat transport in turbulent convection. *Phys. Rev. E* **85**, 016310.

Verzicco, R. & Camussi, R. 1999 Prandtl number effects in convective turbulence. *J. Fluid Mech.* **383**, 55–73.

Wesseling, P. 2000 *Principles of Computational Fluid Dynamics*. Springer-Verlag. 1st ed.

Yee, H. C. 1987 *Upwind and Symmetric Shock-Capturing Schemes*. National Aeronautics and Space Administration/Ames Research Center.

Zhu, X., Mathai, V., Stevens, R. J. A. M., Verzicco, R. & Lohse, D. 2018 Transition to the ultimate regime in two-dimensional Rayleigh–Bénard convection. *Phys. Rev. Lett.* **120**, 144502.